

Resilient Terrain Navigation with a 5 DOF Metal Detector Drone

Patrick Pfreundschuh, Rik Bähnemann, Tim Kazik, Thomas Mantel, Roland Siegwart, and Olov Andersson

Abstract—Micro aerial vehicles (MAVs) hold the potential for performing autonomous and contactless land surveys for the detection of landmines and explosive remnants of war (ERW). Metal detectors are the standard tool, but have to be operated close to and parallel to the terrain. As this requires advanced flight capabilities, they have not been successfully combined with MAVs before. To this end, we present a full system to autonomously survey challenging undulated terrain using a metal detector mounted on a 5 DOF MAV. Based on an online estimate of the terrain, our receding-horizon planner efficiently covers the area, aligning the detector to the surface while considering the kinematic and visibility constraints of the platform. For resilient localization, we propose a factor-graph approach for online fusion of GNSS, IMU and LiDAR measurements. A simulated ablation study shows that the proposed planner reduces coverage duration and improves trajectory smoothness. Real-world flight experiments showcase autonomous mapping of buried metallic objects in undulated and obstructed terrain. The proposed localization approach is resilient to individual sensor degeneracy.

I. INTRODUCTION

Worldwide, landmines and ERW caused more than 7000 casualties in 2020. Member states of the Mine Ban Treaty reported approximately 12 000 km² contaminated, making vast areas uninhabitable [1]. Reducing suspected hazardous areas is challenging, as those areas are inaccessible. Additionally, detecting and mapping potential contamination require expert training. As actual clearance is expensive it should be limited to minimal confirmed hazardous areas [2].

Recently, MAVs with various sensors are being investigated to accelerate land release. A drone can potentially access any terrain without putting a person at risk and automatically collect geo-referenced data. The essential sensor for humanitarian demining is the metal detector. However, implementing a metal detector on a drone has failed so far because of the advanced flight capabilities that are necessary to perform practical surveys.

Detection performance highly depends on the sensor head alignment with the soil surface [3]. Thus, the drone needs to maintain distance while rotating the sensor to align parallel with the surface. This requires the platform to have a customized mechanical concept as well as online perception to resiliently navigate in unknown, obstructed, undulated, outdoor terrain.

In this work, we tackle this challenging surface tracking problem with a novel flying metal detector design. The

This work was supported in part by Armasuisse W+T, in part by Amazon Research Award #4808, and in part by NCCR Dfab P3 through the Swiss National Science Foundation.

Authors are with Autonomous Systems Lab, ETH Zurich, e-mail: {patripfr, brik, tkazik, mantelt, rsiegwart, nandersson}@ethz.ch

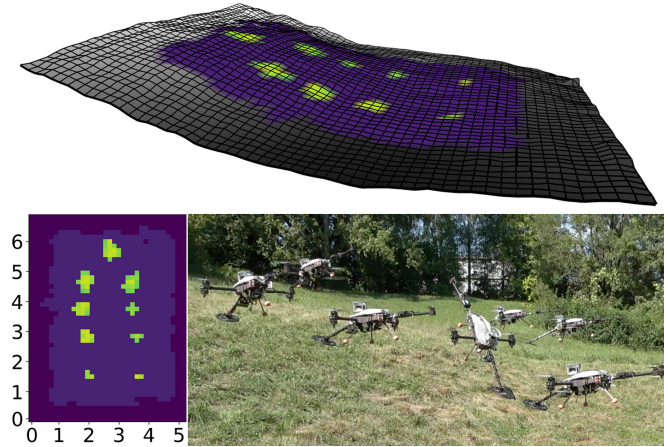


Fig. 1. *Top*: Metal detector signals visualized on a 2.5D terrain map. Colored cells were covered by the sensor. Brighter colors correspond to stronger signal responses from buried objects. *Bottom left*: Top-down 2D detection map. *Bottom right*: The system in action on undulated terrain.

system consists of a 5 DOF drone with a rigidly attached sensor. The drone can maneuver in all three translational directions and independently change its heading and pitch to align the sensor with the surface (see Fig. 1).

However, simply aligning the sensor according to the surface normal is not ideal, as small changes in the normal can cause a large motion of the platform as illustrated in Fig.6. As this is inefficient, we propose a new local trajectory planner that trades off optimal surface alignment with minimal turning efforts and collision avoidance.

During the survey, the system maps the terrain with LiDAR. Precise surface tracking and complete coverage require accurate and smooth localization. However, ERW can be found close to natural or human-made structures that often cause GNSS outages, as well as in feature-less areas which cause drift in LiDAR inertial odometry (LIO). We thus fuse these complementary modalities for resilient localization.

The main contributions of our work are:

- A full system for an autonomous flying metal detector based on a 5 DOF MAV.
- A receding-horizon trajectory planner that optimizes terrain alignment in real-time while considering the drone maneuverability and online map updates.
- Online factor-graph GNSS, IMU and LiDAR localization that is resilient to individual sensor degeneracy.

We show in simulation that our receding-horizon planning reduces coverage duration while maintaining sensor alignment. Real-world experiments show autonomous surveying of undulated and obstructed terrain as well as consistent localization even under the loss of GNSS or drift in LIO.

II. RELATED WORK

A. Flying Robotic ERW Detection

Several efforts have been presented to perform ERW detection using aerial platforms. These systems typically use ground penetrating radars [4]–[6] or cameras [7]. While these sensors can be used to survey large areas from relatively far distances, standardization, as well as target detection, are still being investigated. Yoon et al. [8] use a magnetometer, but require special data processing to detect small objects. The most accepted sensor for deminers is the metal detector. Due to the limited sensing range of metal detectors, it is crucial that the sensor head remains close and parallel to the surface for a strong sensor response [3]. This poses a challenge for regular MAVs, as the attitude of the platform can not be controlled independently of the translation. The Mine Kafon Drone [9] proposed to solve this by mounting the metal detector on a gimbal connected to the drone. However, no results have been reported yet. We present the application of a metal detector that is rigidly mounted to a 5 DOF MAV, which avoids the necessity of a gimbal since the sensor orientation is directly controlled through the pose of the vehicle. Furthermore, our system is the first to perceive the environment online and avoid obstacles.

B. Resilient Online State Estimation with GNSS and LIO

To leverage the complementary nature of GNSS and LIO, both loosely- and tightly-coupled approaches have been proposed. The authors in [10] present a loosely-coupled approach that deploys a dual factor graph to fuse the different modalities. In contrast, [11] uses an extended Kalman filter (EKF) to perform tightly-coupled fusion of LiDAR, inertial, and GNSS measurements. LIO-SAM [12] uses a factor-graph [13] to tightly fuse IMU and GNSS with scan matching LIO. The aforementioned approaches assume that the transformation between the local odometry frame and the GNSS frame is provided. Inspired by visual-inertial GNSS fusion [14]–[16], our approach treats this transformation as an extrinsic calibration that is performed online. Instead of defining it as a constant transformation, we allow it to vary over time to compensate for drift that can accumulate from LIO over periods of GNSS dropouts.

C. Trajectory Planning on Surfaces

Finding the optimal flight trajectory for surface coverage in unknown 3D environments under visibility constraints is a challenging exploration planning problem. Since the full problem is computationally intractable, in this work we assume that a coverage path is given for a region of interest, either from the user or a high-level coverage planner. We then attempt to find a 5 DOF flight trajectory that accurately tracks the terrain surface to ensure good coverage for ERW detection, while also considering its visibility, speed, smoothness and avoiding collisions, in real-time. Earlier work can be broadly categorized into either planning on manifolds without considering coverage, or coverage planning that either does not consider MAV kinematics or runs in real-time. Manifold planning approaches include [17], which uses a

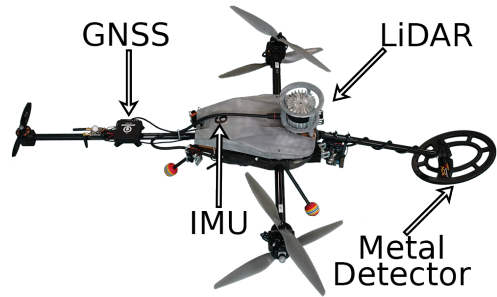


Fig. 2. The Voliro-T tricopter with a custom payload for autonomous navigation and metal detection.

model-predictive control approach, and [18] which proposes a reactive planner based on Riemannian motion policies. Visibility constraints are also included in [19], but do not consider coverage or run in real-time. On the other hand, [20] proposes a belief-space approach to optimize the coverage of free-flight MAV trajectories, but it is vulnerable to local minima and does not run in real-time. Finally, [21] plans coverage patterns high above 3D terrain for a remote sensing application, but does not consider MAV kinematics or appear suitable for real-time flight close to the surface.

III. PLATFORM SETUP

We built our system on top of a tricopter from Voliro AG. The platform, shown in Fig. 2, has fully actuated front propellers, allowing position control independent of the body pitch angle. The additional actuation also improves stable flight near surfaces where disturbances from propeller wash and contact occur. We equipped this platform with an Ouster OS0 128 beam LiDAR with a 90° vertical field of view (FOV), allowing it to observe close terrain. The rear-facing FOV is here partially obscured by the body. LiDAR-based autonomy was highly effective for GNSS-denied indoor navigation in the recent DARPA Subterranean Challenge [22]. We here also use a RTK-GNSS receiver that provides multi-band GNSS from a u-blox ZED-F9P module. A Bosch BMI085 IMU provides the inertial measurements. Finally, a Garret ACE300i metal detector with a main diameter of 0.25 m is rigidly attached at the front. A custom microcontroller interface captures the digital output from the metal detector PCB and sends it to the vehicle’s onboard computer. The software stack runs on an integrated mini PC with an AMD 4800U x86 CPU.

IV. RESILIENT GNSS, IMU AND LiDAR FUSION

A. Notation and Problem Definition

We define a fixed gravity-aligned odometry frame \mathbf{O} . The GNSS receiver measures position with respect to an inertial frame \mathbf{I} , with east-north-up gravity-aligned orientation and origin at the position of the GNSS receiver at the first measurement. The IMU frame serves as the robot body frame \mathbf{B} . The detector frame \mathbf{D} is placed in the center of the metal detector and aligned with the two axes of its ellipse. We define the state of the robot as:

$$\mathbf{x} = [\mathbf{R}_{OB}, \mathbf{O}\mathbf{p}_B, \mathbf{O}\mathbf{v}_{B, B}^a, \mathbf{b}^g]$$

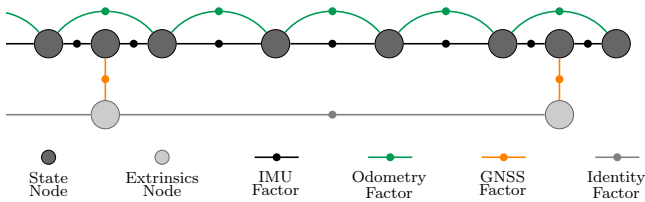


Fig. 3. The factor graph design. State Nodes are connected through Odometry and IMU Factors, while Extrinsic Nodes are connected through Identity Factors. GNSS factors connect State and Extrinsic Nodes.

where $\mathbf{R} \in SO(3)$ and $\mathbf{p} \in \mathbb{R}^3$ represent the body orientation and position. $\mathbf{v}_B \in \mathbb{R}^3$ is its linear velocity, while $\mathbf{b}^a \in \mathbb{R}^3$ and $\mathbf{b}^g \in \mathbb{R}^3$ indicate the accelerometer and gyro biases of the IMU. The extrinsic transformation from the local inertial frame to the odometry frame is denoted as $\mathbf{T}_{OI} \in SE(3)$. The relative position ${}_{B}P_P$ of the GNSS receiver relative to the IMU is assumed to be known. The timestamps of IMU measurements, LiDAR point clouds and GNSS measurements are denoted as t^i, t^j, t^k .

Given the set of LIO estimates, GNSS and IMU measurements the objective is to calculate the maximum a posteriori estimate for a set of states and extrinsics for each timestamp. We formulate this inference problem using the factor graph depicted in Fig. 3. We introduce nodes for the states upon arrival of a new LIO or GNSS measurement, while extrinsic nodes are only introduced at GNSS timesteps. We use a fixed window-length incremental smoothing and mapping (iSAM2) [23] solver to optimize the factor graph. In the following section, we present the individual factors.

B. IMU Factor

Preintegrated IMU factors summarize the IMU measurements between two nodes into a single factor [24]. New state nodes are introduced at GNSS and LiDAR timestamps, which arrive at a lower frequency. We also use the IMU integration as a high-frequency state estimate for flight controller [25].

C. Odometry Factor

Unlike previous LIO-GNSS fusion approaches that rely on features [26], we use FAST-LIO2 [27] as a front-end which operates on points directly. This is favorable in environments with little geometric structure, as raw points can represent subtle features of the scene better. FAST-LIO2 estimates a 6 DOF pose \mathbf{T}_{OB}^j at each t^j . We extract the relative transformation for the odometry factor as,

$$\Delta \mathbf{T}^{j,j+1} = (\mathbf{T}_{OB}^j)^{-1} \mathbf{T}_{OB}^{j+1}.$$

We base the covariance estimation on the constraints of the registration problem, similar to [28], instead of assuming a fixed covariance used in [10], [12]. We calculate the covariance as the inverse of the approximate Hessians,

$$\Sigma_{pos} = \mathbf{H}_{pos} = (\mathbf{J}_{pos}^T \mathbf{J}_{pos})^{-1}, \Sigma_{rot} = \mathbf{H}_{rot} = (\mathbf{J}_{rot}^T \mathbf{J}_{rot})^{-1},$$

where \mathbf{J}_{pos} and \mathbf{J}_{rot} correspond to the translational and rotational components of the measurement Jacobian in [27]. We introduce a tuning constant to scale the covariance.

D. Position Factor

The GNSS receiver measures the position with respect to the inertial frame \mathbf{I} . While the translational components, as well as pitch and roll of the extrinsics to the fixed frame \mathbf{O} can be directly observed, the yaw is only observable after the platform has moved sufficiently. We treat this transformation as an additional variable that is estimated in the factor graph. We formulate the measurement model as:

$${}_{I}P_P = (\mathbf{T}_{OI})^{-1} \cdot \mathbf{T}_{OB} \cdot {}_{B}P_P.$$

Position factors update the state and the extrinsics. We use the measurement covariance provided by the GNSS receiver.

E. Initialization

Initially, the vehicle is static to estimate an initial value for the IMU biases and gravity alignment. We initialize the extrinsics with a high covariance on the yaw. Until the covariance of the yaw of the extrinsics is below a threshold, we artificially increase the GNSS measurement covariance to enforce that GNSS measurements have a negligible impact on the state estimate before the yaw is sufficiently observed.

V. ELEVATION MAPPING USING LiDAR

The sensor head is supposed to closely track the surface. This requires an accurate representation of the local terrain. Due to the limited FOV, not all relevant terrain can be estimated from a single point cloud. Additionally, this would result in a very noisy map in the presence of vegetation. To this end, we use the 2.5D grid map framework presented in [29]. It efficiently fuses 3D measurements using a Kalman filter. It is also used to calculate surface normals for the tracking, in addition to a 3D signed distance field (SDF) used for collision avoidance. The platform should avoid obstacles such as large rocks, trees, or poles as they are unlikely to contain landmines or ERW. We identify traversable areas using a threshold on the slope of the terrain.

VI. TRAJECTORY PLANNER FOR SURFACE TRACKING

To ensure reliable detection of buried objects, the metal detector head has to be parallel to the ground surface.

While our actuated 5 DOF drone can align with any surface by using a combination of yaw $\psi(t)$ and pitch $\theta(t)$, this results in many inefficient yaw changes over uneven terrain as seen in Fig. 6. This also does not ensure that the next segment of the coverage pattern has been sufficiently mapped by the LiDAR sensor.

We therefore need to plan a trajectory over position and orientation, $(\mathbf{p}(t), \mathbf{R}(t))$, that minimizes control effort (e.g. turning) to ensure smooth and efficient trajectories while satisfying ground alignment constraints, the kinematic limits for the MAV, in addition to LiDAR visibility constraints guaranteeing that it does not fly into unknown space.

To make this difficult optimization problem amenable to solution in real-time, we first show how to simplify it for a 5 DOF MAV without obstacles, then we add a collision avoidance strategy.

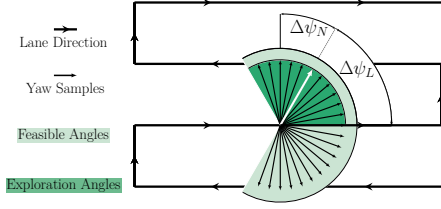


Fig. 4. Illustration of the final reduced planning problem on a coverage path. A state lattice is constructed from yaw samples along the path, which have to satisfy sensor visibility constraints (light green) of $\pm 120^\circ$ around the direction of flight. Dark green samples are preferred as they ensure visibility of the next lane as well.

Since the translational dynamics of the actuated MAV are fast compared to the maximum speed of 1 m/s allowed for reliable detection with a metal detector [30], we can assume that the coverage path can be tracked in position and just optimize rotations along the path.

At each discrete time step t^n we therefore want to solve a receding-horizon trajectory planning problem over the next h meters of the coverage path, which can be formalized as an optimal control problem from t^n ,

$$\begin{aligned} \min_{\mathbf{R}(\cdot)} \quad & J = \int_{t^n}^{t^h} c(\dot{\mathbf{R}}(t)) dt & (1) \\ \text{subj. to} \quad & \dot{\mathbf{R}}(t) < \mathbf{R}_{\max}, & \text{(kinematic limits)} \\ & \alpha(t) < \alpha_{\max}, & \text{(surface alignment)} \\ & |\Delta\psi_L(t)| < \Delta\psi_{L_{\max}}, & \text{(forward visibility)} \\ & \mathbf{R}(t^n) = \hat{\mathbf{R}}_{t^n}, & \text{(current orientation)} \\ & \mathbf{R}(t) \in SO(3), & \forall t \in [t^n, t^h], \end{aligned}$$

where t^h is the time at h meter into the path, $\Delta\psi_L(t)$ is the angle between the MAV and lane headings as shown for a boustrophedon coverage pattern in Fig. 4, and finally $\alpha(t)$ is the ground alignment error as defined in Fig. 5a.

We also exploit that one can analytically derive the optimal pitch as a function of the yaw. The alignment error α shown in Fig. 5a is defined as the shortest angle between the surface normal and the z axis of the detector frame,

$$\alpha(\theta) = \cos^{-1}(\mathbf{o}\mathbf{n} \cdot (\mathbf{R}_{OD}(\theta) \cdot \mathbf{D}\mathbf{z}_D)) = \cos^{-1}(f(\theta)). \quad (2)$$

The optimal pitch θ^* for a yaw ψ is therefore

$$\theta^*(\psi) = \tan^{-1} \left(\frac{n_x \cos(\psi) + n_y \sin(\psi)}{n_z} \right). \quad (3)$$

For the proof, see Appendix I. This allows us to further reduce the trajectory optimization problem in (1) to just solving for the optimal yaw trajectory $\psi(\cdot)^*$. Finally, as we are aiming for a smooth trajectory in terms of yaw, we define the cost function to minimize yaw changes $c(\dot{\mathbf{R}}(t)) = \dot{\psi}(t)$.

A. Approximate Solution via Graph Search

At each discrete planner iteration t^n , we find an approximate solution to the planning problem in (1) by incrementally constructing a state lattice [31], and finding the minimum cost trajectory via graph search. The lattice is constructed by

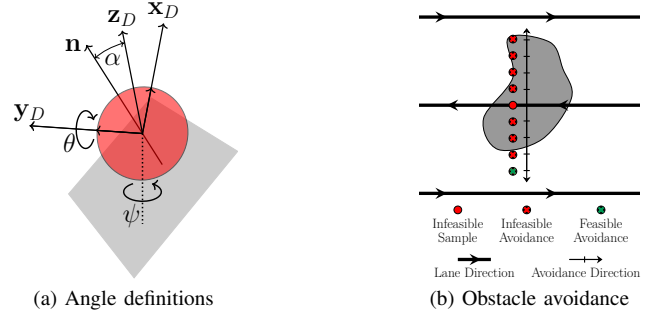


Fig. 5. *Left:* Illustration of the axes and angles to compute the optimal pitch given a candidate yaw angle. The grey square represents a surface cell and the red circle the metal detector plane. *Right:* A grey obstacle invalidates the initial sample. If no collision-free trajectory can be found, we incrementally generate avoidance samples in the two perpendicular directions to the lane direction until a feasible trajectory is found.

discretizing the coverage path into reference positions. Given one discrete sample (x_{ref}^l, y_{ref}^l) , we fix the 3D position

$$\mathbf{o}\mathbf{P}_D^l = [x_{ref}^l, y_{ref}^l, z_{ref}^l]^T + d \cdot \mathbf{o}\mathbf{n}. \quad (4)$$

Here d is the desired distance to the surface, $\mathbf{o}\mathbf{n} \in \mathbb{R}^3$ is the surface normal, and z_{ref} is the surface elevation. We then sample yaw angles, as illustrated in Fig. 4 with a resolution of 3° to create a candidate tuple $(\mathbf{o}\mathbf{P}_D^l, \psi_j^l)$. For each tuple we attempt to connect it to all feasible tuples in the previous step t^{l-1} , checking that the motion satisfies the constraints in (1), as well as checking collisions and traversability against the elevation map using the SDF defined in Section V. Together these define a multitree $\mathcal{G} = \{\mathcal{V}, \mathcal{E}\}$. Nodes \mathcal{V}_l at layer l represent the lattice states at the planning step t^l , and are connected to \mathcal{V}_{l-1} through edges $E(v) = \{e(v, v')\}_{v' \in N(v)}$. The cost along each edge is the change in yaw. The minimum cost path through the lattice is efficiently found via breadth-first graph search. At each planning iteration, we only sample nodes for the new layer and reuse the previous tree.

B. Exploration

To incentivize exploration of the *next* lane, we first solve the optimization problem (1) under the additional constraint

$$|\Delta\psi_N(t^h)| < e_{\max} \quad \text{(exploration constraint)}$$

where ψ_N is the direction that points towards the next lane as seen in Fig. 4. This constraint is relaxed if no feasible solution with an exploration state was found, which can be efficiently implemented in the graph search approach by just checking the last layer in the search tree.

C. Collision Avoidance

In practice, obstacles may block parts of the coverage path. To maintain the same graph search formulation while handling this problem, our algorithm pushes the sampled path position out of the obstacle as shown in Fig. 5b. For all infeasible positions \mathbf{p}^j in $[t^n, t^h]$ on the discretized state lattice, we iteratively sample avoidance positions orthogonal away from the coverage path until the position is feasible. We then plan a trajectory over this collision-free (sub-optimal) path using the graph-search approximation above.

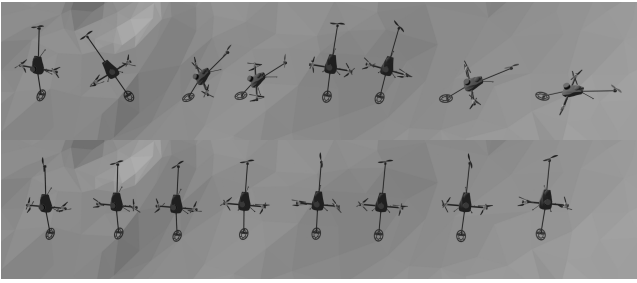


Fig. 6. One lane in irregular but mostly flat simulated terrain. *Top*: With the naive *Aligned-1* approach the platform does inefficient turning along the lane. *Bottom*: With the proposed planner, the system can translate along the lane with only slight changes to its orientation.

VII. EXPERIMENTAL RESULTS

In the following section, we conduct several experiments to demonstrate the performance of the presented system. We first analyze the proposed planning approach quantitatively in a simulation environment. We then conduct three real-world flight experiments to evaluate the resilience of the sensor-fusion approach, and finally the full system for autonomous detection of metallic objects buried in the ground using the metal detector. To integrate the detector signal, we identify measured cells in the grid map by ray tracing from the four bounding points and the center of the sensor to the map. We recommend the video submitted alongside this paper for additional visualization of this section.

A. Trajectory Planner for Surface Tracking

To evaluate the performance of our planner, we simulate the drone using a Gazebo model with the same dimensions, LiDAR sensor and controller as the real platform. We deploy the system in a scaled-down model of a crater landscape [32] that exhibits different types of irregular terrain that we are interested in for ERW surveys. The $25 \times 10\text{m}^2$ survey area starts in a mostly flat but irregular terrain that is followed by a curved slope and ends in an irregular, undulated area.

In addition to the proposed planner, we also simulate three baseline approaches as an ablation study. The first baseline approach (*Aligned-1*) is a greedy surface tracker that only samples the two orientations that align perfectly with the surface and set the planning horizon to one step, i.e. $h = 0.3\text{m}$. The second baseline (*Aligned-6*) samples the same orientations but uses a similar planning horizon as our approach, i.e. $h = 1.8\text{m}$. The third baseline (*Fixed Attitude*) is roughly equivalent to an underactuated quadcopter that ignores the slope of the terrain and simply follows the surface with a fixed height offset. We simulate this using the 5 DOF MAV but set $\psi = \theta = 0$ and mount the metal detector in the middle of the platform. Note that this will result in improved results compared to an actual quadcopter, as the platform can still translate without pitching. All approaches use ground truth odometry. The parameters for the experiment are listed in Tab. I and the results are shown in Tab. II. To calculate alignment quality, for each cell we find the best observed alignment α_{min} over all poses on the flight trajectory, and calculate the average over all cells, denoted as $\bar{\alpha}_{min}$.

The *Fixed Attitude* method is a lower limit on how fast the area can be covered, given the translational velocity

TABLE I

PARAMETERS USED FOR THE PRESENTED EXPERIMENTS

		Simulation		Real-World		
Lane spacing	0.2 m	h	1.8 m	v_{max}	1 m/s	0.6 m/s
Sample spacing	0.3 m	α_{max}	7.5°	ω_{max}	60°/s	30°/s
Grid cell size	0.15 m	$\Delta\psi_{L_{max}}$	120°	d	0.15 m	0.18 m

TABLE II

PLANNER PERFORMANCE IN SIMULATION. MEAN, STANDARD DEVIATION AND 95TH PERCENTILE ARE INDICATED BY $\bar{\cdot}$, σ AND 95TH.

Method	Duration [s]	$\bar{\Delta\psi_{t^n}} \pm \sigma$ [°]	$\bar{\Delta\theta_{t^n}} \pm \sigma$ [°]	$\bar{\alpha}_{min}$ [°]	α_{min}^{95th} [°]
Fixed Attitude	2132	0.0 ± 0.0	0.0 ± 0.0	11.38	24.29
Aligned-1	2502	31.28 ± 65.06	2.70 ± 2.55	1.76	4.15
Aligned-6	2469	28.07 ± 58.15	2.68 ± 2.56	1.74	4.14
Proposed	2208	4.17 ± 17.17	2.94 ± 3.64	3.41	7.25

constraint. Our proposed approach only takes 3.6% longer compared to this, while it is able to cover the area in 10.6% less time than the *Aligned-6* approach and has a much smoother trajectory in terms of yaw, as visible in Fig. 6. On average the yaw change between subsequent target poses, $\bar{\Delta\psi_{t^n}}$, is decreased by 23.9° compared to *Aligned-6*, while the average pitch change $\bar{\Delta\theta_{t^n}}$ is only marginally increased.

As the *Fixed Attitude* baseline does not track the orientation of the surface, the metal detector is poorly aligned in uneven areas, resulting in a 95th percentile of α_{min} of 24.29°, which does not allow for reliable detection. Note that this result is a lower bound on rigidly mounting it to a regular quadcopter, and would become even worse for more inclined areas. As expected our approach has a higher alignment deviation than the *Aligned* approaches. However, the 95th percentile of our approach stays below the intended limit of 7.5° while covering the terrain more efficiently. In contrast to our approach, all compared approaches traversed unobserved terrain multiple times.

B. Resilient GNSS-IMU-LiDAR Localization

To evaluate the proposed resilient sensor fusion approach, we deployed our system in an outdoor environment that contains both a GNSS-denied area and an area where LIO undergoes severe drift. FAST-LIO2 measurements arrive at

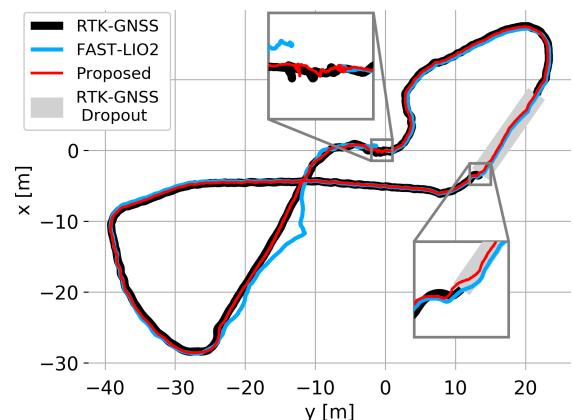


Fig. 7. XY-plot of the localization experiment. *Bottom Detail*: RTK-GNSS recovery. The proposed approach estimates a consistent trajectory during RTK-GNSS loss and remains smooth upon recovery. *Top Detail*: Start/End Point. The FAST-LIO2 trajectory is not closed due to accumulated drift, while start and end point of the proposed approach match.

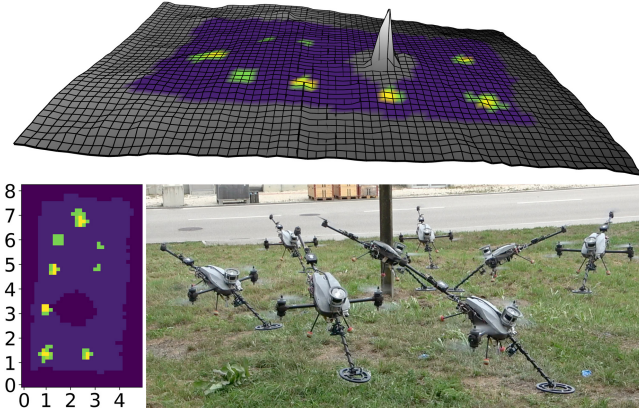


Fig. 8. *Top*: Metal detector signals visualized on a 2.5D terrain map. Colored cells were covered by the sensor. *Bottom left*: Top-down 2D detection map. *Bottom right*: The system in action maneuvers around the obstacle while maintaining detector alignment.

20 Hz while RTK-GNSS measurements arrive at 5 Hz. We use a window length of 5 s. A pilot steered the platform manually in position control mode using the state estimation feedback presented in Sec. IV. After takeoff, the extrinsics \mathbf{T}_{OI} converged after approximately 3.5 m. The drone first flies through a dense tree canopy which causes RTK-GNSS loss and later traverses a large flat grassland which causes FAST-LIO2 to drift. To evaluate the drift, the platform was started and landed in the same position with an accuracy of approximately 0.15 m. As visualized in Fig. 7 the proposed approach retains a locally consistent state estimate while traversing through the RTK-GNSS-denied area that remains smooth upon signal recovery. FAST-LIO2 deviates 4.2 m from the RTK-GNSS trajectory in an area where the point cloud registration is underconstrained. Since we calculate the LIO covariance based on the geometric structure, our approach implicitly handles the degeneracy and closely follows the RTK-GNSS trajectory. The total estimated distance between the take-off and landing position of our approach is 0.18 m. This is within our landing accuracy, while the final distance estimated by FAST-LIO2 is 1.52 m.

C. Autonomous Search for Buried Metallic Objects

We evaluate the complete system in two real-world experiments. As metallic targets, we used gas cartridges with a diameter of 0.1 m. They were buried in the ground to be leveled with the surface to facilitate inspection of the results.

In the first experiment we deploy the system in an undulated terrain covered by grass with a main slope of around 20° and steeper local inclinations along multiple axes. We placed 9 metallic targets. The platform covered the target area of $5.5 \times 4 \text{ m}^2$ in 317 s. As illustrated in Fig. 1, the planner generates trajectories that enable the sensor head to track the surface orientation. Additionally, despite the terrain steepness, the drone always avoids collisions with any part of the body. We visualize the average sensor response over all values in a cell of the created map in Fig. 1. The 9 metallic objects are clearly visible. The lateral distance between the objects matches the actual distance of 1.65 m by visual inspection. It can be seen that the patches with

high-intensity are larger than the actual objects. Note that given the working principle of the sensor, this is expected as one measurement represents the whole area under the sensor head. Thus, even a tiny object can cause high-intensity measurements of the size of the metal detector.

In a second experiment, we test the obstacle avoidance of the proposed system. We deploy the system in an environment with a main slope of around 8° which is slightly sloping downwards to both sides. A large metal pole is present in the survey area. We placed 9 metallic targets. The platform covered the target area of $7 \times 3.5 \text{ m}^2$ in 373 s. The planner identifies the pole as an obstacle and successfully maneuvers around it while maintaining the sensor head aligned to the surface, as shown in Fig. 8. 8 metallic targets can be identified in the generated map. The remaining target was placed in an area close to the pole that was not traversed by the detector due to obstacle avoidance.

VIII. CONCLUSIONS

We presented a complete system for metal detection with a 5 DOF MAV. The system is capable of navigating in GNSS denied and LIO degenerate environments and adjusts its coverage trajectory based on terrain, visibility, and obstacles. The maneuverability of the platform shows superior surface tracking over an underactuated MAV. The proposed receding-horizon planner ensures good terrain perception and improved coverage progress over compared approaches. Our real-world experiments showcase that the proposed system is able to autonomously survey challenging undulated terrain for ERW detection. The visualization of the metal detector response on the terrain map combined with the GNSS reference allows for easy re-localization of the hazardous areas for demining. Even though we here focused on ERW detection, our resilient surface navigation could also be extended to other surface tracking applications such as spraying, close-up imaging or non-destructive testing.

APPENDIX

A. Derivation of θ_{cand}^*

We search θ that minimizes the alignment error α given ψ :

$$\theta_{cand}^* = \arg \min_{\theta} \alpha(\theta) = \arg \max_{\theta} f(\theta) \quad (5)$$

$$f(\theta) = \mathbf{o}\mathbf{n} \cdot (\mathbf{R}_{OD}(\theta, \psi) \cdot D\mathbf{z}_D) \stackrel{\text{Roll} \perp 0}{=} \sin(\theta) \underbrace{(n_x \cos(\psi) + n_y \sin(\psi))}_a + \cos(\theta)n_z \quad (6)$$

We find the critical point as:

$$f(\theta_c)' = \cos(\theta_c)a - \sin(\theta_c)n_z \stackrel{!}{=} 0 \Leftrightarrow \theta_c = \tan^{-1}\left(\frac{a}{n_z}\right) = \tan^{-1}\left(\frac{n_x \cos(\psi) + n_y \sin(\psi)}{n_z}\right) \quad (7)$$

$$f(\theta)'' = -\sin(\theta)a - \cos(\theta)n_z \stackrel{!}{<} 0 \stackrel{\cos(\theta) > 0}{\Leftrightarrow \theta \in (-\pi, \pi)} -\tan(\theta)a < n_z^2 \quad (8)$$

Inserting (7) into (8) yields:

$$-\tan(\tan^{-1}\left(\frac{a}{n_z}\right))a = -a^2/n_z < n_z \stackrel{n_z > 0}{\Leftrightarrow} -a^2 < n_z^2 \quad (9)$$

Since $f(\theta_c)' = 0$ and $f(\theta_c)'' < 0$ we find $\theta_{cand}^* = \theta_c$

REFERENCES

- [1] International Campaign to Ban Landmines, “Landmine Monitor 2021,” 2021.
- [2] United Nations Mine Action Service (UNMAS), “IMAS 07.11 - Land Release,” 2019.
- [3] European Committee for Standardization, “Humanitarian Mine Action - Test and evaluation - Metal Detectors,” 2003.
- [4] R. Bähnmann, N. Lawrance, L. Streichenberg, J. J. Chung, M. Pantic, A. Grathwohl, C. Waldschmidt, and R. Siegwart, “Under the Sand: Navigation and Localization of a Micro Aerial Vehicle for Landmine Detection with Ground-Penetrating Synthetic Aperture Radar,” *Field Robotics*, vol. 2, no. 1, pp. 1028–1067, Mar. 2022.
- [5] Y. A. Lopez, M. Garcia-Fernandez, G. Alvarez-Narciandi, and F. L.-H. Andres, “Unmanned aerial vehicle-based ground-penetrating radar systems: A review,” *IEEE Geoscience and Remote Sensing Magazine*, 2022.
- [6] D. Sipos, P. Planinsic, and D. Gleich, “On drone ground penetrating radar for landmine detection,” in *2017 First International Conference on Landmine: Detection, Clearance and Legislations (LDCL)*, 2017, pp. 1–4.
- [7] J. Baur, G. Steinberg, A. Nikulin, K. Chiu, and T. S. de Smet, “Applying deep learning to automate uav-based detection of scatterable landmines,” *Remote Sensing*, vol. 12, no. 5, p. 859, 2020.
- [8] L.-S. Yoo, J.-H. Lee, Y.-K. Lee, S.-K. Jung, and Y. Choi, “Application of a Drone Magnetometer System to Military Mine Detection in the Demilitarized Zone,” *Sensors*, vol. 21, no. 9, p. 3175, Jan. 2021, number: 9 Publisher: Multidisciplinary Digital Publishing Institute.
- [9] M. Hassani. Mine Kafon. (2022, August 30).
- [10] J. Nubert, S. Khattak, and M. Hutter, “Graph-based Multi-sensor Fusion for Consistent Localization of Autonomous Construction Robots,” in *2022 International Conference on Robotics and Automation (ICRA)*, May 2022, pp. 10 048–10 054.
- [11] X. Li, H. Wang, S. Li, S. Feng, X. Wang, and J. Liao, “GIL: a tightly coupled GNSS PPP/INS/LiDAR method for precise vehicle navigation,” *Satellite Navigation*, vol. 2, no. 1, p. 26, Nov. 2021.
- [12] T. Shan, B. Englot, D. Meyers, W. Wang, C. Ratti, and D. Rus, “Lio-sam: Tightly-coupled lidar inertial odometry via smoothing and mapping,” in *2020 IEEE/RSJ International Conference on Intelligent Robots and Systems (IROS)*, 2020, pp. 5135–5142.
- [13] F. Dellaert and M. Kaess, 2017.
- [14] R. Mascaro, L. Teixeira, T. Hinzmann, R. Siegwart, and M. Chli, “GOMSF: Graph-Optimization Based Multi-Sensor Fusion for robust UAV Pose estimation,” in *2018 IEEE International Conference on Robotics and Automation (ICRA)*, May 2018, pp. 1421–1428, iSSN: 2577-087X.
- [15] S. Boche, X. Zuo, S. Schaefer, and S. Leutenegger, “Visual-Inertial SLAM with Tightly-Coupled Dropout-Tolerant GPS Fusion,” Aug. 2022, arXiv:2208.00709 [cs].
- [16] W. Lee, K. Eickenhoff, P. Geneva, and G. Huang, “Intermittent GPS-aided VIO: Online Initialization and Calibration,” in *2020 IEEE International Conference on Robotics and Automation (ICRA)*, May 2020, pp. 5724–5731, iSSN: 2577-087X.
- [17] G. Lu, W. Xu, and F. Zhang, “Model predictive control for trajectory tracking on differentiable manifolds,” *arXiv preprint arXiv:2106.15233*, 2021.
- [18] M. Pantic, L. Ott, C. Cadena, R. Siegwart, and J. Nieto, “Mesh manifold based riemannian motion planning for omnidirectional micro aerial vehicles,” *IEEE Robotics and Automation Letters*, vol. 6, no. 3, pp. 4790–4797, 2021.
- [19] M. Watterson, S. Liu, K. Sun, T. Smith, and V. Kumar, “Trajectory optimization on manifolds with applications to quadrotor systems,” *The International Journal of Robotics Research*, vol. 39, no. 2-3, pp. 303–320, 2020.
- [20] B. Davis, I. Karamouzas, and S. J. Guy, “C-opt: Coverage-aware trajectory optimization under uncertainty,” *IEEE Robotics and Automation Letters*, vol. 1, no. 2, pp. 1020–1027, 2016.
- [21] Y. Choi, Y. Choi, S. Briceno, and D. N. Mavris, “Three-dimensional uas trajectory optimization for remote sensing in an irregular terrain environment,” in *2018 International Conference on Unmanned Aircraft Systems (ICUAS)*. IEEE, 2018, pp. 1101–1108.
- [22] M. Tranzatto, M. Dharmadhikari, L. Bernreiter, M. Camurri, S. Khat-tak, F. Mascarich, P. Pfreundschuh, D. Wisth, S. Zimmermann, M. Kulkarni, V. Reijgwart, B. Casseau, T. Homberger, P. De Petris, L. Ott, W. Tubby, G. Waibel, H. Nguyen, C. Cadena, R. Buchanan, L. Wellhausen, N. Khedekar, O. Andersson, L. Zhang, T. Miki, T. Dang, M. Mattamala, M. Montenegro, K. Meyer, X. Wu, A. Briod, M. Mueller, M. Fallon, R. Siegwart, M. Hutter, and K. Alexis, “Team cerberus wins the darpa subterranean challenge: Technical overview and lessons learned,” 2022.
- [23] M. Kaess, H. Johannsson, R. Roberts, V. Ila, J. Leonard, and F. Dellaert, “isam2: Incremental smoothing and mapping with fluid relinearization and incremental variable reordering,” in *2011 IEEE International Conference on Robotics and Automation*, 2011, pp. 3281–3288.
- [24] C. Forster, L. Carlone, F. Dellaert, and D. Scaramuzza, “On-manifold preintegration for real-time visual–inertial odometry,” *IEEE Transactions on Robotics*, vol. 33, no. 1, pp. 1–21, 2017.
- [25] V. Indelman, S. Williams, M. Kaess, and F. Dellaert, “Information fusion in navigation systems via factor graph based incremental smoothing,” *Robotics and Autonomous Systems*, vol. 61, no. 8, pp. 721–738, 2013.
- [26] J. Zhang and S. Singh, “Loam: Lidar odometry and mapping in real-time,” in *Robotics: Science and Systems*, vol. 2, no. 9. Berkeley, CA, 2014, pp. 1–9.
- [27] W. Xu, Y. Cai, D. He, J. Lin, and F. Zhang, “Fast-lid2: Fast direct lidar-inertial odometry,” *IEEE Transactions on Robotics*, vol. 38, no. 4, pp. 2053–2073, 2022.
- [28] J. Zhang, M. Kaess, and S. Singh, “On degeneracy of optimization-based state estimation problems,” in *2016 IEEE International Conference on Robotics and Automation (ICRA)*, 2016, pp. 809–816.
- [29] P. Fankhauser, M. Bloesch, and M. Hutter, “Probabilistic terrain mapping for mobile robots with uncertain localization,” *IEEE Robotics and Automation Letters (RA-L)*, vol. 3, no. 4, pp. 3019–3026, 2018.
- [30] Garrett Electronics Inc. (2016) Ace 300i owner’s manual.
- [31] M. Pivtoraiko, R. A. Knepper, and A. Kelly, “Differentially constrained mobile robot motion planning in state lattices,” *Journal of Field Robotics*, vol. 26, no. 3, pp. 308–333, 2009.
- [32] R. Jaumann, D. A. Williams, D. L. Buczkowski, R. A. Yingst, F. Preusker, H. Hiesinger, N. Schmedemann, T. Kneissl, J. B. Vincent, D. T. Blewett, B. J. Buratti, U. Carsenty, B. W. Denevi, M. C. D. Sanctis, W. B. Garry, H. U. Keller, E. Kersten, K. Krohn, J.-Y. Li, S. Marchi, K. D. Matz, T. B. McCord, H. Y. McSween, S. C. Mest, D. W. Mittlefehldt, S. Mottola, A. Nathues, G. Neukum, D. P. O’Brien, C. M. Pieters, T. H. Prettyman, C. A. Raymond, T. Roatsch, C. T. Russell, P. Schenk, B. E. Schmidt, F. Scholten, K. Stephan, M. V. Sykes, P. Tricarico, R. Wagner, M. T. Zuber, and H. Sierks, “Vesta’s shape and morphology,” *Science*, vol. 336, no. 6082, pp. 687–690, 2012.